Available on CMS information server

CMS NOTE 2000/009

The Compact Muon Solenoid Experiment

CMS Note

Mailing address: CMS CERN, CH-1211 GENEVA 23, Switzerland

01 February 2000

Analysis from August 1999 beam tests of a PbWO4 Crystal matrix

P. Depasse, J. Donini, J-P. Ernenwein, J. Fay, S. Gascon, B. Ille, T. Schumm[a)], F. Zach

Institut de Physique Nucléaire de Lyon, Lyon, France

Abstract

One 6×5 lead tungstate crystal matrix has been tested during the August 1999 SPS test beam period . This note resumes the main results concerning electronic noise, correlated noise, light yield, capsules gain, energy resolution in clusters of 9 crystals, scan in positions. At the end, a comparison between data and simulation is given to evaluate performance.

[a)] CERN Summer Student

1 Introduction

The CMS collaboration has chosen lead tungstate crystals as the active medium for its electromagnetic calorimeter. Beam tests have been performed since 1995 in order to determine the performance of this crystal and the associated electronics. In August 1999, data were taken in the H4 testbeam facility with a matrix of 6×5 crystals, with final mechatronics.

2 Experimental set-up in August 1999

The matrix tested in August was a 6×5 array of $PbWO_4$ crystals. The dimensions of these crystals were the final ones expected for the ECAL : $22.0 \times 22.0\, mm^2$ for the front face, $26.0 \times 26.0\, mm^2$ for the rear face and $230\, mm$ in length. Each crystal was in an alveolar structure. The 30 crystals were surrounded by a set of 4 thermalised copper plates which enabled temperature control via Lauda cooling system. The temperature was fixed at $18^oC \pm 0.1^oC$. The capsules were glued on the rear crystal faces with Histomount glue. A capsule is a mechanical and eletronic structure with 2 APDs in parallel (see figure 9). Each APD has a 75 pF capacitance. Capsules have been mounted and tested at IPN Lyon. Temperature sensors (AD590) were mounted on 2 capsules of each sub-module of 10 crystals.

Each of 3 submodules has a different kind of signal transmission cables. For sub-module 1, signals are transmitted between APDs and electronics by shielded cables ; for sub-module 2, kaptons from NFlex with Nicomatic connectors and for sub-module 3, kaptons from Avi-Peschard with Berg connectors.

Behind the matrix, we find 3 electronic cards for 10 channels, each with FPPA (final version but with only gain 8) and QADC. The next figures show the set-up (cf. Fig. 1 and 2).

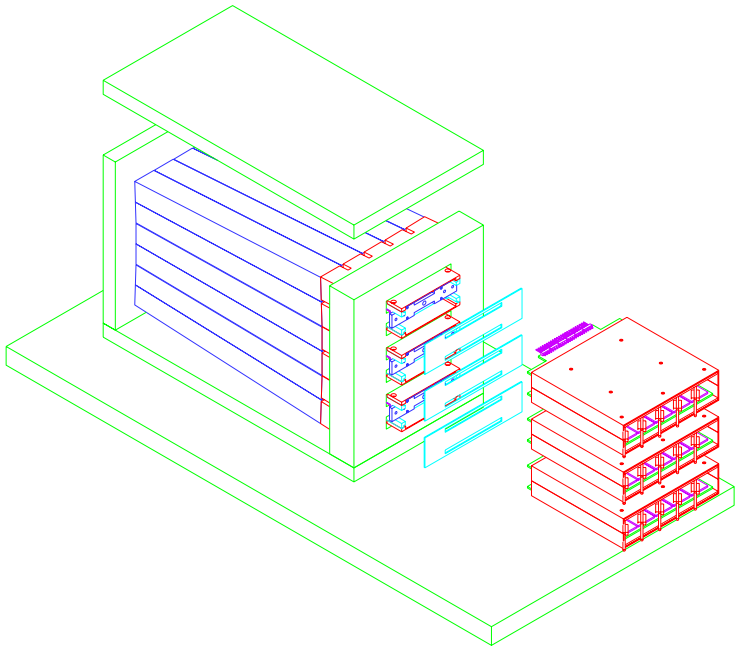

Figure 1: View of prototype 99 in H4

For these tests, we use the final mechatronics (nez-de-cartes).

Optical fibers were connected at the front end of the matrix for monitoring crystals with green laser light (480 nm). There is also an electronic test pulse to monitor each electronic card.

For this period, the matrix was tilted by 3^o each in θ and ϕ.

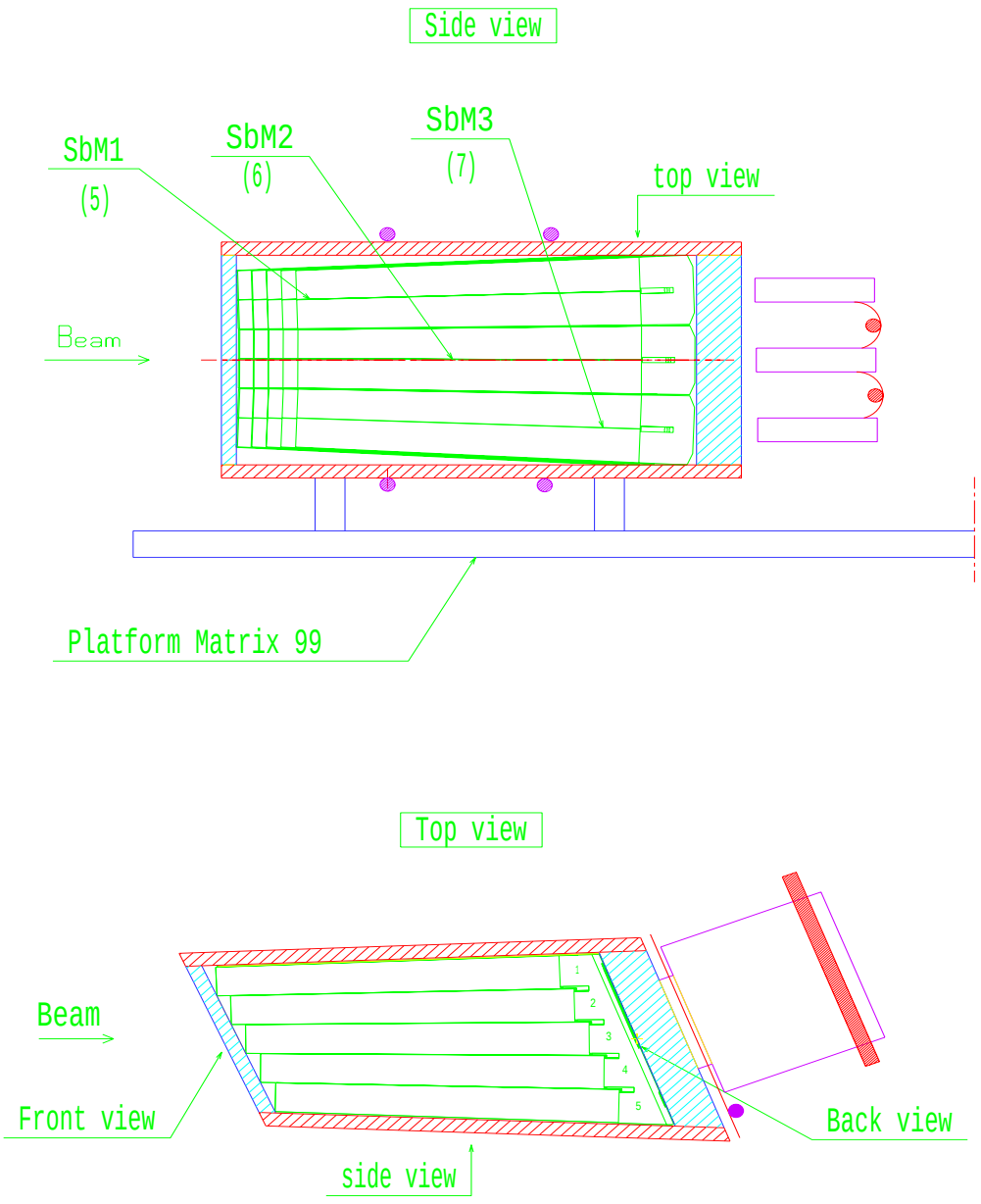

Figure 2: View of prototype 99 in H4

3 Electronic Noise

We distinguish 2 periods during the August runs : the first 10 days at the beginning dedicated to noise and energy resolution and the second 10 days for high-energy runs and differents tests (high voltage, ...). During both periods, to see all the signals, we had to put some attenuators on the patch panel. So we distinguish, for noise estimation, runs with and without attenuators.

3.1 Noise by channel

We can estimate electronic noise with electron or muon beams or with a test pulse :

- electron or muon beams : ADC channels corresponding to the deposited energy give a calibration coefficient K. Using the pedestal witdh, we determine noise in MeV.
- test pulse : due to the input capacitance (1 pF), a ADC channel represents $3.12 \times 10^6\ e-$.

Figures 3 and 4 show distributions of noise estimated by electron beam and test pulse for 29 channels. Channel 1 has some connector problems, so we can't determine its noise.

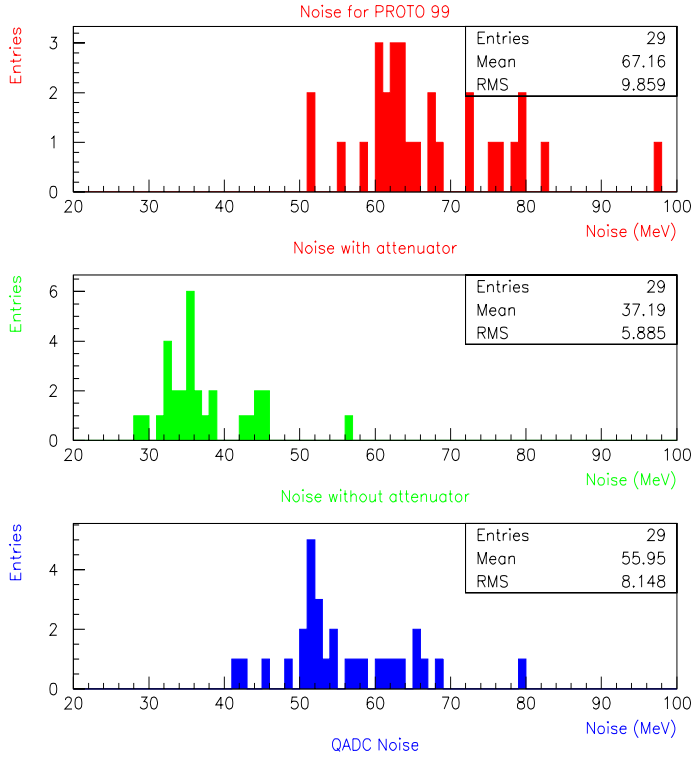

Figure 3: Noise estimated by electron beam

In each figure, there are 3 sub-figures. The 2 sub-figures on top show the distribution of noise with/without attenuator. We then, by calculating the quadratic difference, determine QADC noise, shown in the sub-figure on bottom. We can see that the QADC noise is very important here.

Figure 5 shows the same distributions for some channels where a muon beam was used. In this case, the 2 figures on top show distribution with or without an gain of 100, necessary to see a clear signal. With amplification, mean noise is within 2σ of that obtained using the electron beam without attenuator. The QADC noise is clearly cut whithout attenuators on patch pannel.

In conclusion, we have the following mean noise :

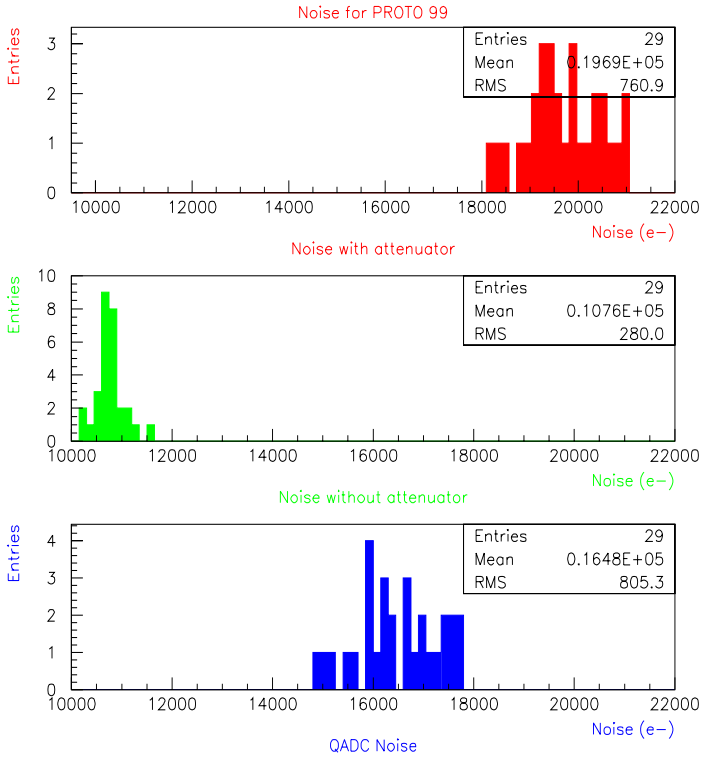

Figure 4: Electronic noise estimated by test pulse

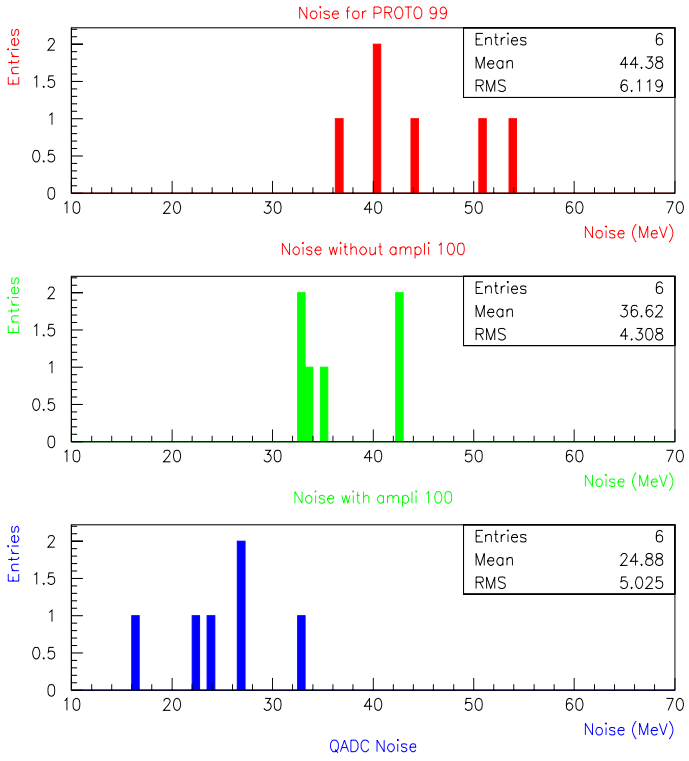

Figure 5: noise estimated with muon beam

	Noise(MeV)	Noise(e^-)
With att.	67.2	19690
QADC	56.0	16480
Without att.	37.2	10760

The next table shows the value and the dispersion of noise (in MeV) for all runs when attenuators were used :

1	**2**	**3**	**4**	**5**
	75.0	63.6	60.7	63.6
	2.14	2.32	1.48	1.40
6	**7**	**8**	**9**	**10**
67.5	57.2	61.3	52.8	62.6
1.85	1.46	1.12	1.22	4.63
11	**12**	**13**	**14**	**15**
77.3	52.1	80.3	81.3	64.7
1.97	1.32	2.49	2.33	1.80
16	**17**	**18**	**19**	**20**
69.0	63.6	59.1	62.8	68.3
2.00	2.15	1.53	1.84	2.05
21	**22**	**23**	**24**	**25**
64.2	62.6	64.3	64.0	82.7
2.23	1.33	1.78	2.28	2.29
26	**27**	**28**	**29**	**30**
69.3	96.6	80.7	71.8	77.7
1.80	2.53	1.97	2.07	1.89

For sub-module 1, there was (channels 2-10) a mean noise of 62.9 MeV, for sub-module 2, 68.0 MeV and for sub-module 3, 73.2 MeV. The explanation for the fact that the upper sub-module was less noisy than the others is that the upper electronic card is the reference ground for the whole prototype.

We can also examine the distribution of noise for all runs during a period. Figure 6 shows the distribution of noise for one channel (crystal 22). We see a good stability, with a mean noise of 46.7 MeV and a witdh of 1.33 MeV for 132 entries.

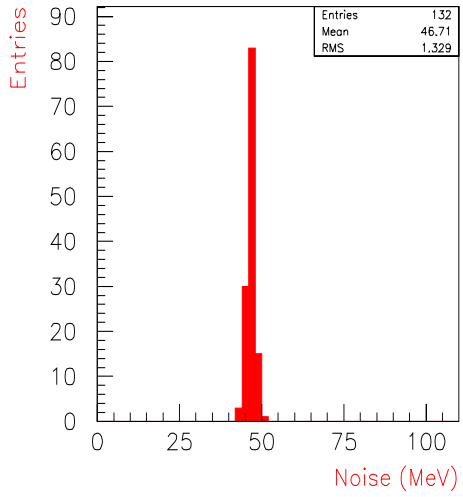

Figure 6: Distribution of noise for channel 22 during period 2

We can also compare for the 2 periods the ratio rms of noise to noise for all channels. Figures 7 and 8 show these distributions. The mean value are the same : 2.9% with a width of 0.94% for period 1 and 0.82% for period 2.

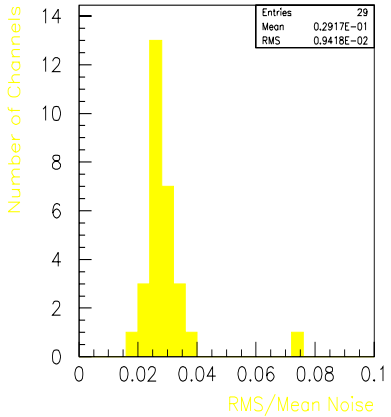

Figure 7: Ratio RMS/noise for all channels, period 1

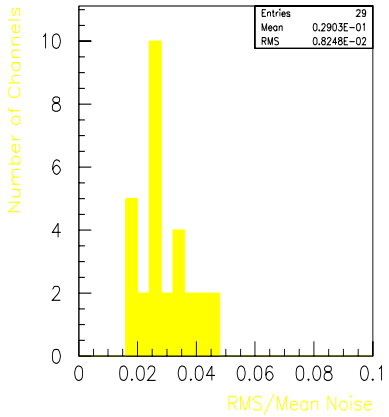

Figure 8: Ratio RMS/noise for all channels, period 2

3.2 Correlated Noise

To estimate correlated noise, the following formula is used:

$$\sigma_c = \frac{\sigma_{sum}^2 - \sum_{i=1}^{N} \sigma_i^2}{N(N-1)}$$

where σ is the pedestal width and N the number of considered channels.

There are many possibilities in a 6×5 matrix to have correlated noise. The most relevant are the following :

- By sub-module :

  We have used the data taken with attenuators for this calculation.

Sub-Module 1	Sub-Module 2	Sub-Module 3
16.7 MeV	12.2 MeV	17.1 MeV
5430 e^-	3500 e^-	4510 e^-

  Sub-module 2 appears to have a lower correlated noise than the others.

- For all channels : For this study, we use runs taken without attenuators, since the results of these calculations will be used forward to estimate intrinsic noise.

$$\sigma_c = 8\ MeV\ or\ 2200\ e^-$$

  Since this value is insignificant, it seems that matrix is well screened.

3.3 Intrinsic Noise

The intrinsic noise can be estimated by quadratic subtraction between the noise without attenuators and the correlated noise :

$$< B > = 36.3\ MeV\ or\ 10530\ e^-$$

Expressed in electrons, this level of noise is expected, since at IPNL, the noise for electronics cards was measured to be approximately $10000\ e^-$. In MeV, it is a value consistent with that stated in the TDR.

4 Capsules with 2 APDs

In fig. 9, a capsule is shown with its kapton liaison and connector, 2 APDs and a temperature sensor. At IPNL, we have tested 30 capsules at $\simeq\ 23^oC$. Therefore, for the H4 runs at 18^oC, we have applied a correction in order to estimate the bias voltage corresponding to gain 50.

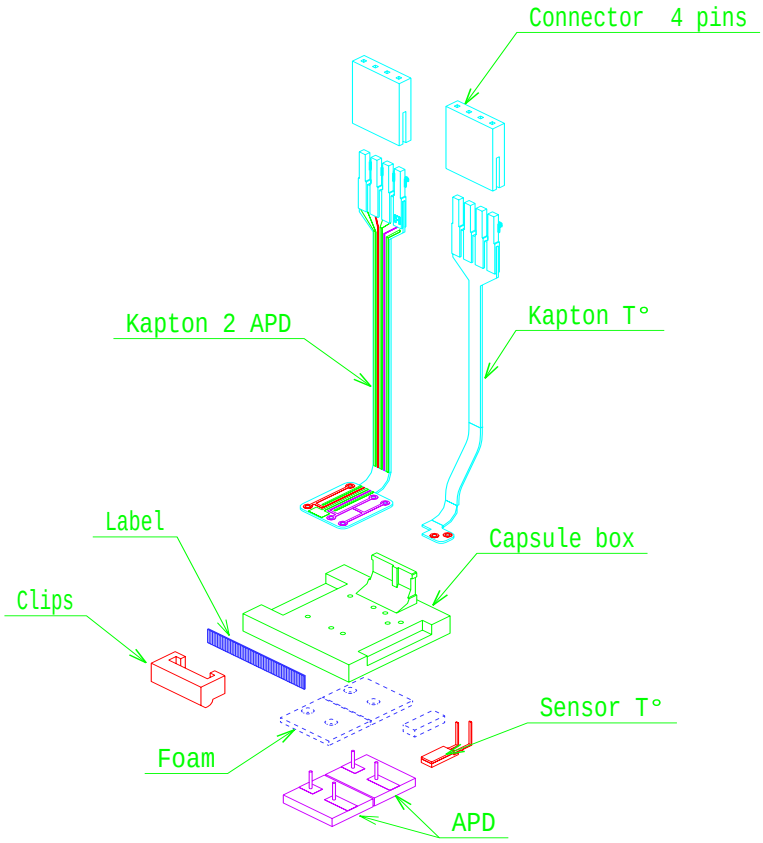

Figure 9: Exploded view of a capsule with temperature sensor

4.1 Capsule Gain

To monitor gain in situ, we use the following method. At each bias value, we calculate the following ratio :

$$R\ =\ \frac{Laser/Pin}{Pulse/Pin}$$

The value of laser normalized to a PIN diode is proportional to the photocurrent delivered by the capsule. We correct by test pulse to account for distorsion of pulse shape at low voltage.

Then we determine the reference gain (G=1) by a mean with points at 40, 60 and 80 V. In figure 10, we can see that normalization by 2 reference PINs of the monitoring system give the same gain. We obtain a mean gain of 50.8 with PIN0 and 51.1 with PIN1. Both RMS are very large, so we can consider that both methods give effectively the same result.

In figure 11, distributions of capsules gain during 2 periods of August are shown. We do gain measurements at the beginning and the end of each period. The mean gain is very stable (see following table). The bias was chosen at $318.0 \pm 1.0\ V$ and the mean gain is 50.1 ± 3.4 during August runs.

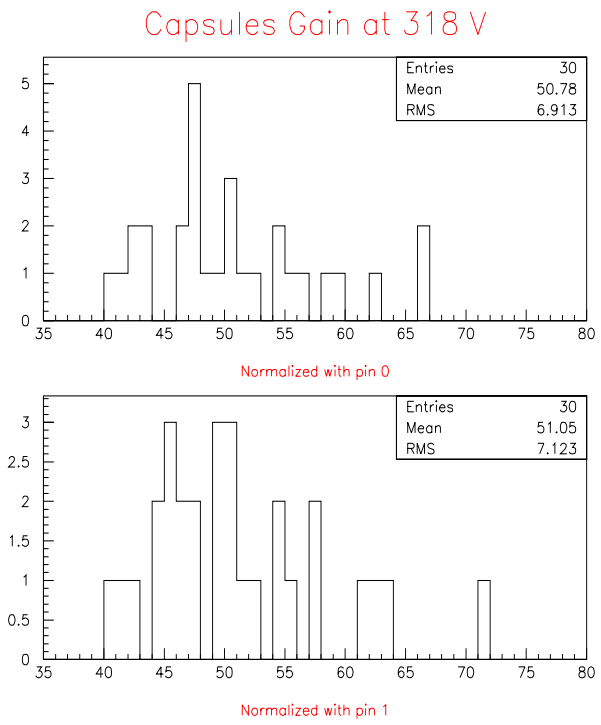

Figure 10: 2 types of normlization thanks to monitoring system at 318 V

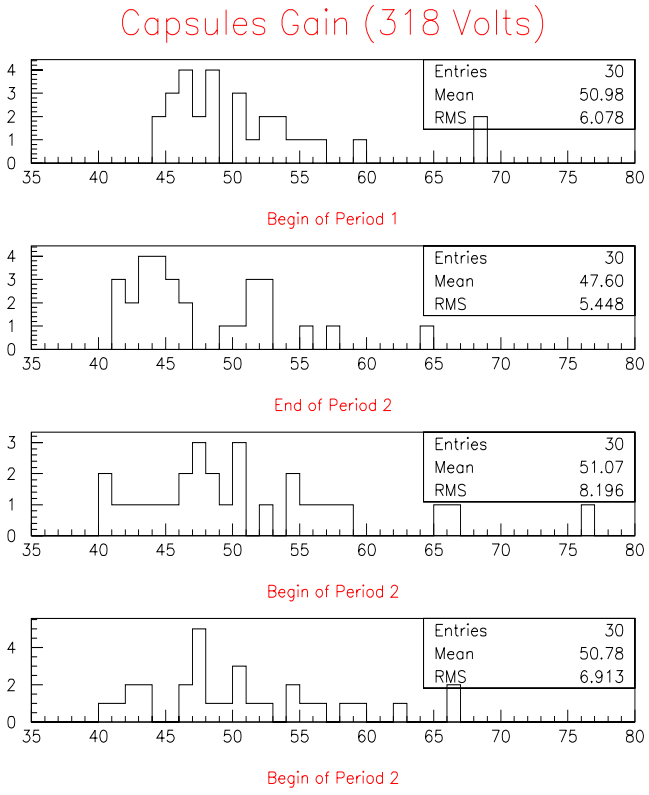

Figure 11: Distributions of capsules gain during 2 periods at 318 V

	¡Gain¿	RMS
Beginning of period 1	51.0	6.1
End of period 1	47.6	5.4
Beginning of period 2	51.1	8.2
End of period 2	50.8	6.9

We have done a comparison between measurements done at IPNL and in situ during the August runs. As previously mentionned, the measurements done at IPNL were at $23^o\ C$. To deduce an equivalent value of the IPNL gain at $18^o\ C$ and 318 V , we estimate the gain at 318 V from the IPNL measurements then corrected this value by a factor of $2.5\%/^o\ C$. Figure 12 shows a comparison of the distributions of the capsule gains between IPNL and H4.

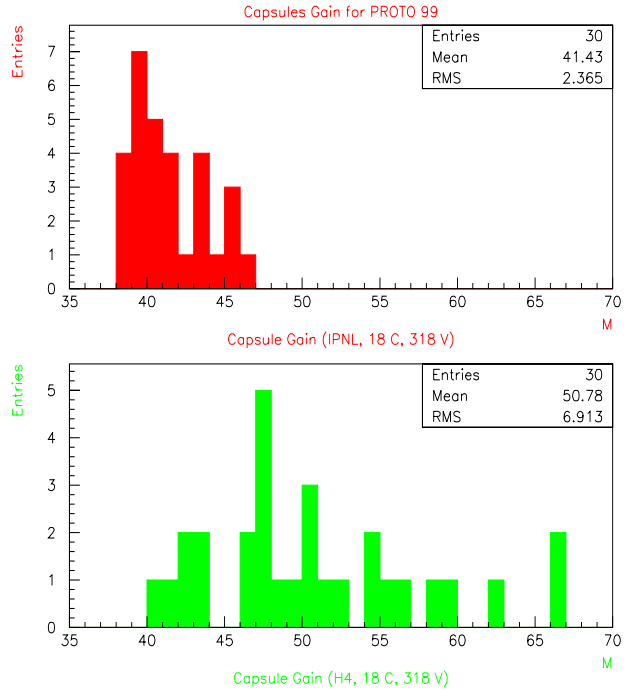

Figure 12: Comparison of capsule gains between IPNL and H4

The distributions are clearly different both in mean value and dispersion. The difference is probably related to the high voltage supply used and needs to the further understood.

Figure 13 shows bias distribution to obtain gain 50 at $18^o\ C$, deduced from IPN measurements. It's another way to verify a discrepancy between IPN and H4.

The bias for M=50 and $18^o\ C$ is : $322 \pm 2\ V$. In H4, we have the same bias for all capsules : $318 \pm 1\ V$. We obtain the same conclusion as before : we don't retrieve same gain between IPN and H4 with same bias.

4.2 Visualization of APDs

Thanks to the nuclear counter effect from charged MIP interacting in the silicium, we can see APDs of a capsule during runs with a muon beam. Figure 14 shows crystal display with a little box of $5 \times 5\ mm^2$. It's one of the two APDs of the capsule. Due to the 3^o tilt, we can't see the second APD. This is verified in figure 15, in which the same quantity are displayed, only for a simulated prototype in same conditions (cf. section Simulation) as in beam (3^o tilt in θ and ϕ).

4.3 Light Yield

To evaluate the crystals light yield, we use the capsule gain (cf. section Gain), calibration constants in MeV and in e^- :

$$LY\ =\ \frac{1}{M} \times \frac{K(e^-)}{K(MeV)}$$

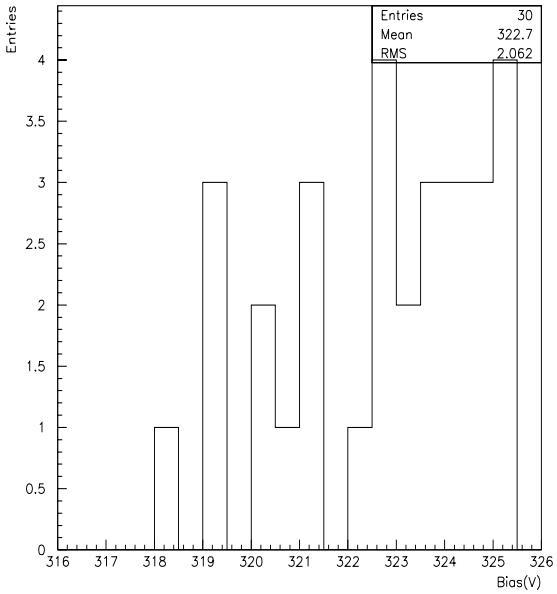

Figure 13: Voltage distribution corresponding to M=50 and 18^o C deduced from the IPN measurements

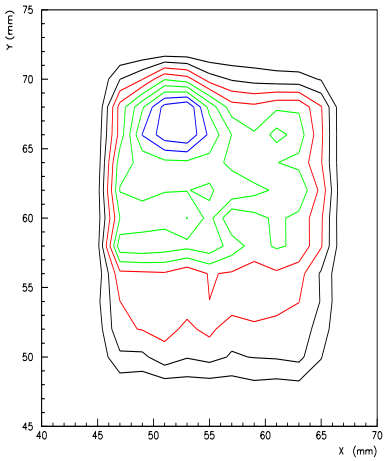

Figure 14: Visualisation of one APD of a capsule in the muon beam data from August 1999

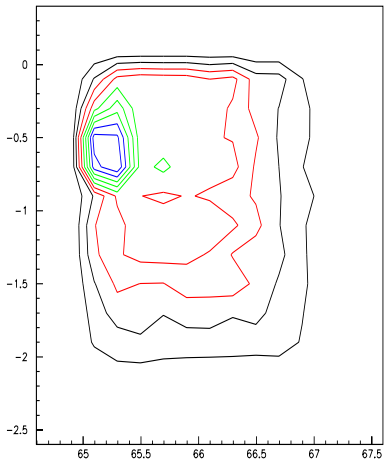

Figure 15: Visualisation of one APD of a capsule in the muon beam simulation

with :

- $K(e^-)$ calibration constant in $e^-/ADC\ channel$
- $K(MeV)$ calibration constant in $MeV/ADC\ channel$

The Light Yield value is in pe/MeV. To compare values between beam test and ACCOS measurements (found in CRYSTAL database), we use the same product $\epsilon_Q \times MF$ where ϵ_Q is quantum efficiency (13% for PM in ACCOS and $\simeq\ 80\%$ for APDs) and MF is the matching factor ($=\ 1$ for PM used by ACCOS and $(2 \times 25\ mm^2)/(\simeq (25.75\ mm)^2)$ for 2 APDs behind a crystal of type 6).

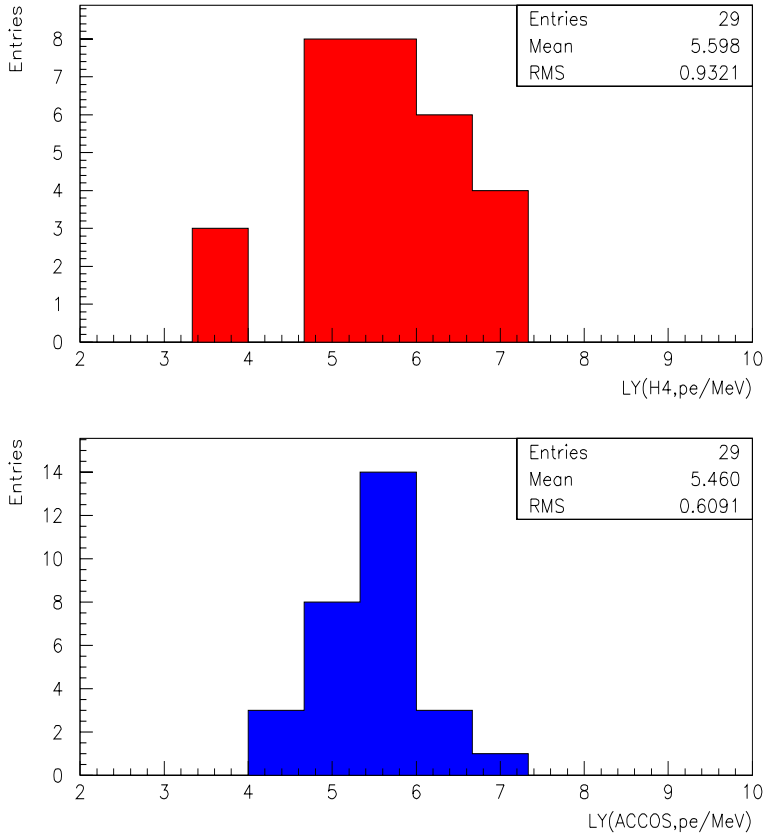

Figure 16: Light Yield measured from beam test (up) and on ACCOS machine (down)

Figure 16 shows that we find similar values in both measurements :

$$L.Y. \simeq 5.5\ \pm\ 0.6\, pe^-/MeV$$

5 Energy resolution

5.1 Set-Up

During the 2 August runs, we have calculated energy resolution under several different scenarios. In the first run,the beam energies were between 15 and 150 GeV with 2 attenuation setups :

- all crystals of a sub-matrix (9 crystals) have the same attenuation factor
- only the central crystal in a sub-matrix has an attenuator

This last choice allows to reduce noise (cf. section Electronic Noise).

In the second run, the beam energies were between 150 and 280 GeV with 2 bias setups :

- capsule bias at 318 V

- capsules with bias at 314 V, because at $E_{beam} = 280\ GeV$, a bias at 318 V induced saturation of some preamplifier.

During the next 2 sections, we show only the results for the central crystal with attenuator for the range 15 to 150 GeV and the bias at 314 V for range 150 to 280 GeV.

5.2 Range 15 to 150 GeV

The beam energies commonly used for these tests were 15, 20, 35, 50, 80, 120 et 150 GeV. We considered only 11 of the 12 possible 'sum of 9' sub-matrices in proto '99 (because channel 1 was dead,so we could not use channel 7 as the central crystal for the sum of 9).

We used a $4\times4mm^2$ triggering beam area centered on the central crystal of the array studied. We fit all distributions (pedestal and signal) by a gaussian. The procedure to obtain energy resolution at each beam energy value was the following :

- sum of 9 crystals in pedestal and signal
- fit (gaussian) of the 2 distributions

Then we do a fit of the function $\sigma(E)/E$ versus E where :

$$\sigma^2 = a^2 \times E \oplus b^2 \times E^2 \oplus c^2$$

and :

* σ is the signal width from the gaussian fit
* E is the reconstructed beam energy
* a : stochastic coefficient
* b : constant term
* c : noise (= pedestal witdh)

Figures 17 and 18 show distributions of signal and noise for crystal 22 at 50 and 120 GeV (beam energy).

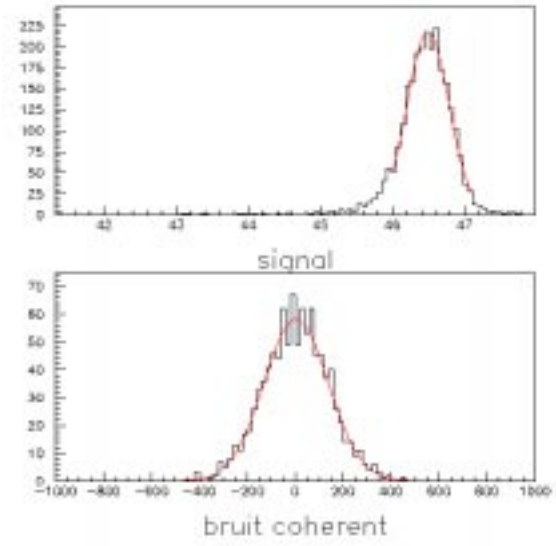

Figure 17: Reconstructed energy (in GeV) and noise (so called 'bruit coherent') for 50 GeV in crystal 22

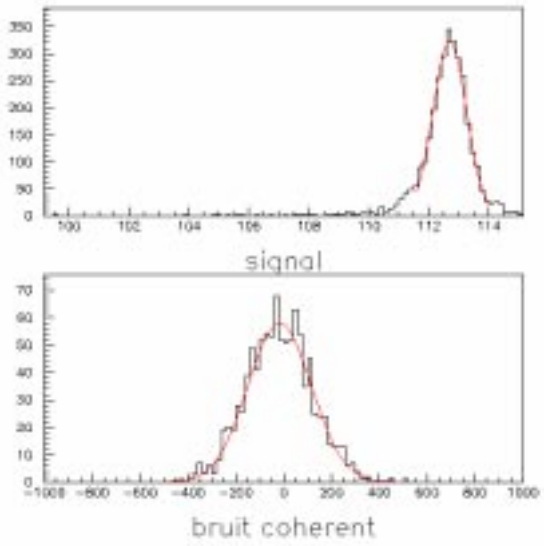

Figure 18: Reconstructed energy (in GeV) and noise (so called 'bruit coherent') for 120 GeV in crystal 22

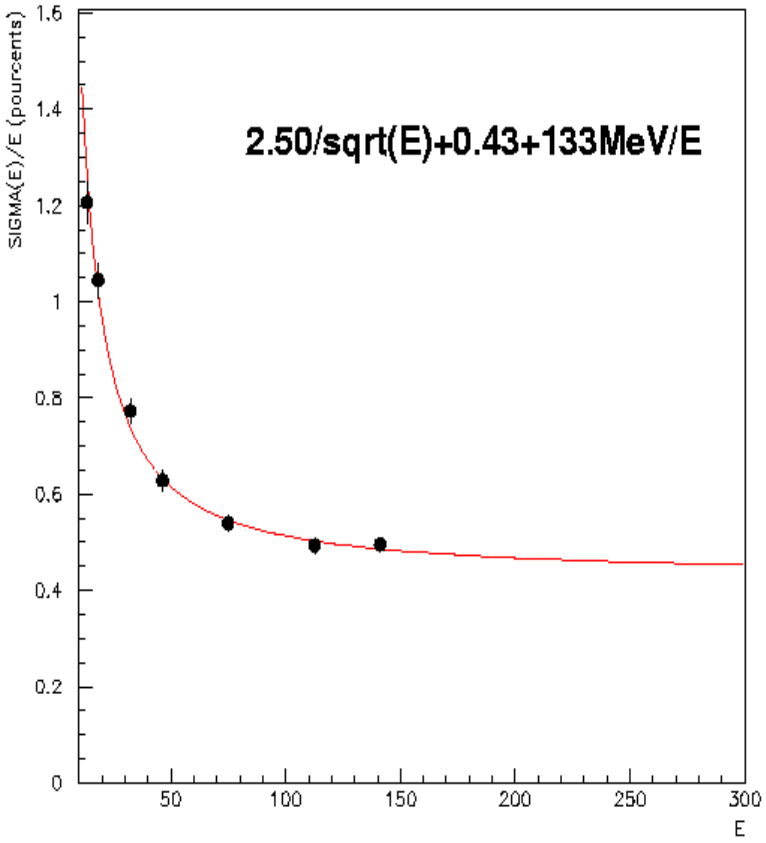

Figure 19: Energy resolution for period 1 and crystal 22

Figure 19 shows the energy resolution obtained with the fit. The noise term, including the contribution from correlated noise, has been subtracted before the fit.

Figure 20 shows distributions of energy resolution fit parameters for all 11 sub-matrices. We can see that the stochastic coefficents are very similar.

The *mean* parametrized energy resolution for period 1 is :

$$\frac{\sigma}{E} = \frac{2.69\%}{\sqrt{E}} \oplus 0.42\% \oplus \frac{133\ MeV}{E}$$

5.3 Linearity

To study the linearity of the electronics, we use peak values (in ADC channels) for all energies. A fit between peak values and nominal beam energies is done and the difference between data and fit for each energy value is evaluated :

$$diff = \frac{Peak - Fit}{Peak}$$

Figures 21 and 22 show 2 distributions for a single crystal :

- top : peak versus beam energy, with fit
- bottom : difference versus beam energy

Figure 21 contains all energy values and figure 22 all excepting $E_{beam} = 15\ GeV$.

The maximum percentage difference between data peak and fit varies by a factor of 2 depending on whether the point at 15 GeV is included or not. Figure 23 shows distributions for 12 central crystals of maximal difference (as defined in figure 21) between data and fit in the 2 cases : 15 to 150 GeV and 20 to 150 GeV.

The 'mean maximal difference' is $1.6\ \%$ for range 15 to 150 GeV and $0.9\ \%$ for range 20 to 150 GeV.

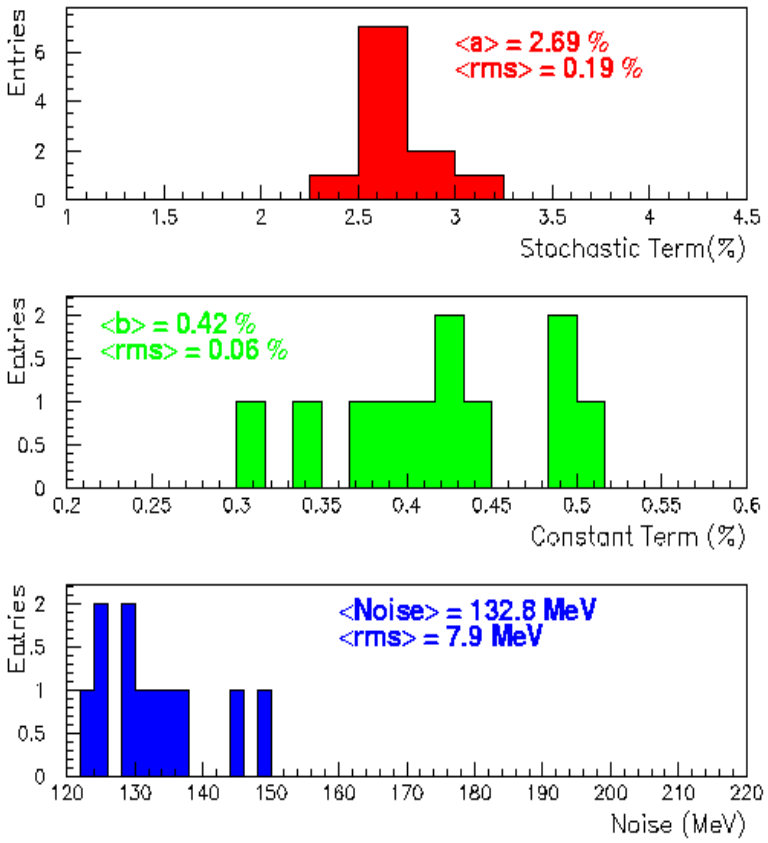

Figure 20: Distributions of energy resolution fit parameters for period 1

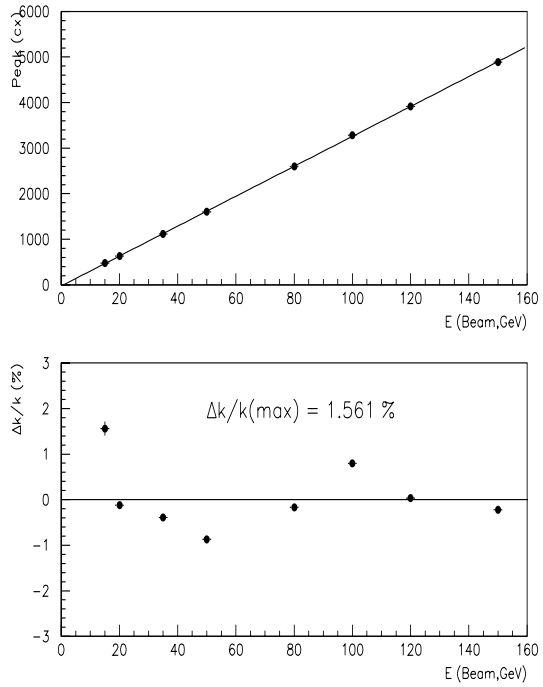

Figure 21: Linearity for crystal 22 and range 15 to 150 GeV

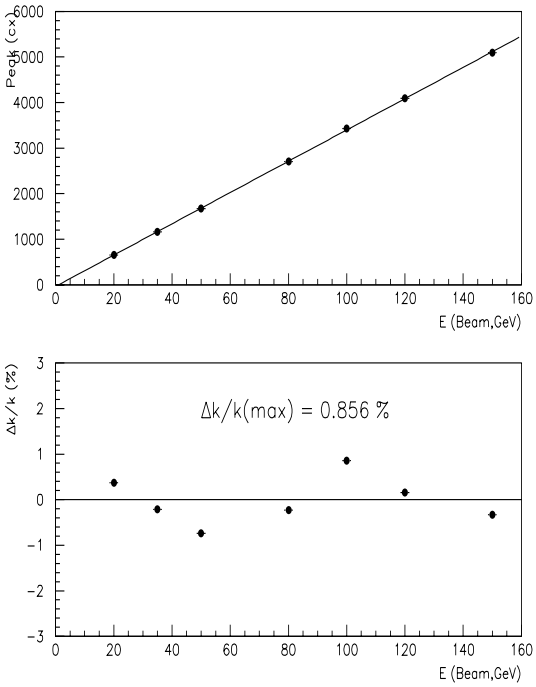

Figure 22: Linearity for crystal 23 and range 20 to 150 GeV

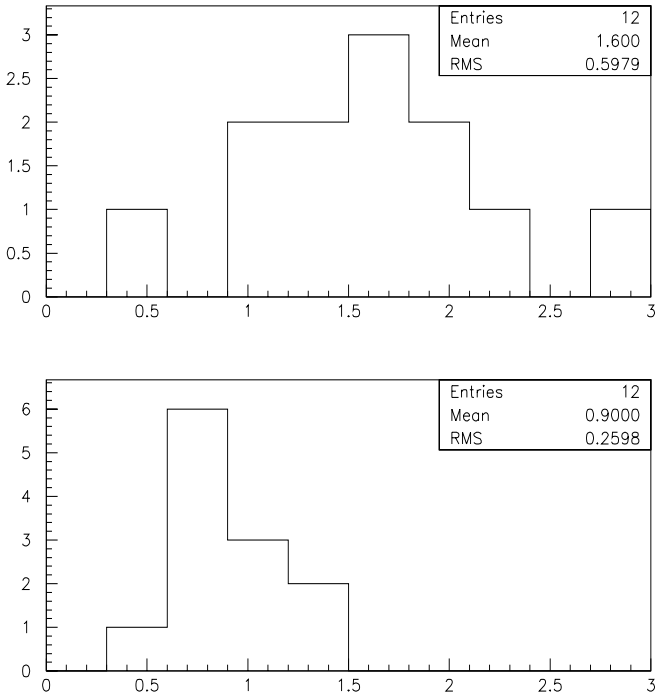

Figure 23: Distributions of maximal gap in percentage between data and fit for the range (15,150) and (20,150) GeV

5.4 Range 150 to 280 GeV

During period 2, we only use the highest available energies : 120,200 and 280 GeV. To fit the energy resolution, we now constrain the fit with the stochastic term found previously for the lower energy range. In fact, this run is useful for evaluation of the constant term (the fit must be drived with stochastic term for low energies).

Figures 24 and 25 show the distributions of signal and noise at 120 and 280 GeV for crystal 18. We can see that a gaussian seems to be a appropriate fit for these distributions.

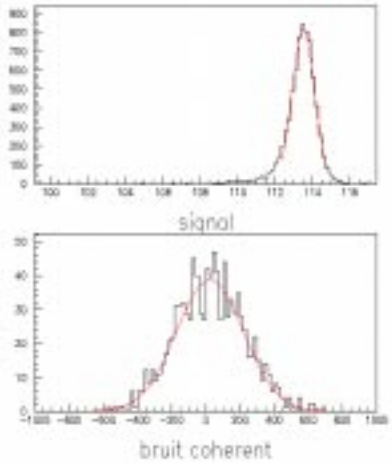

Figure 24: Distributions of the reconstructed energy (in GeV) and noise (so called 'bruit coherent') for 120 GeV in crystal 18

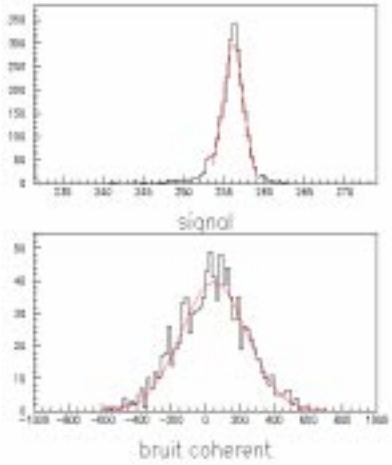

Figure 25: Distributions of the reconstructed energy (in GeV) and noise (so called 'bruit coherent') for 280 GeV in crystal 18

Figure 26 shows energy resolution obtained by the fit on crystal 18. The noise is higher as expected, due to the presence of higher attenuation factors on each crystal.

In the same way as for period 1, figure 27 shows distributions of energy resolution fit parameters for period 2 and for all 11 crystals.

The *mean* energy resolution for period 2 is :

$$\frac{\sigma}{E} = \frac{2.69\%}{\sqrt{E}} \oplus 0.43\% \oplus \frac{203\ MeV}{E}$$

5.5 Combination of Ranges

We can combine the resolution and noise of periods 1 and 2 to make a single fit between 15 and 280 GeV. We use the same method as previously. Since the noise value changes significantly between periods 1 and 2, we emphasize that the overall noise value gived is the mean of all values.

Figure 28 shows the energy resolution for crystal 18 in the entire energy range.

Figure 29 shows distributions of the energy resolution parameters only for 6 of the possible 11 central crystals ; for the remaining 5 crystals, there was a preamp saturation problem at 280 GeV. Therefore, it was not possible to reconstruct the correct deposited energy ; the values found were below $92\ \%$ of the beam energy. So we fit the combined energy resolution only on 6 good central crystals.

The *mean* energy resolution for the 2 August periods over the entire energy range is :

$$\frac{\sigma}{E} = \frac{2.75\%}{\sqrt{E}} \oplus 0.38\% \oplus \frac{150\ MeV}{E}$$

If we do the same fit for both August periods, but without including the point at 280 GeV, we obtain the distributions of the energy resolution parameters for 11 crystals shown in figure 30.

The mean parameters change very little (with the exception of the noise, expected to be higher).

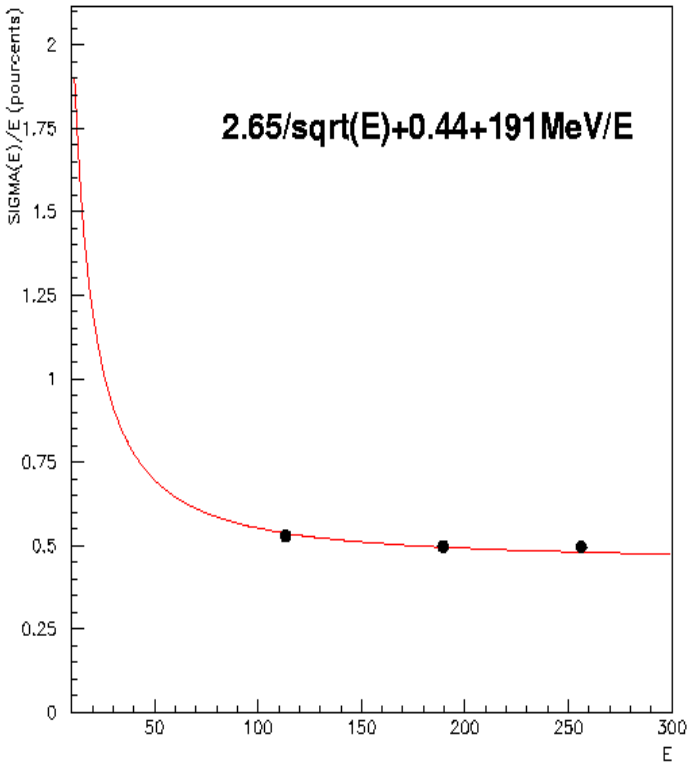

Figure 26: Energy resolution for period 2 and crystal 18

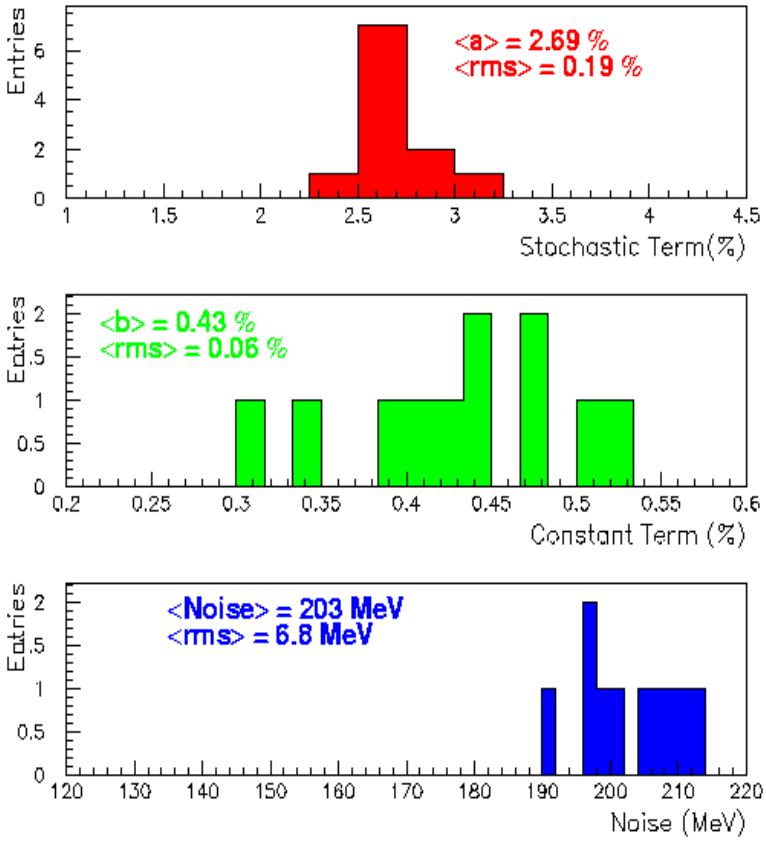

Figure 27: Distributions of energy resolution fit parameters for period 2

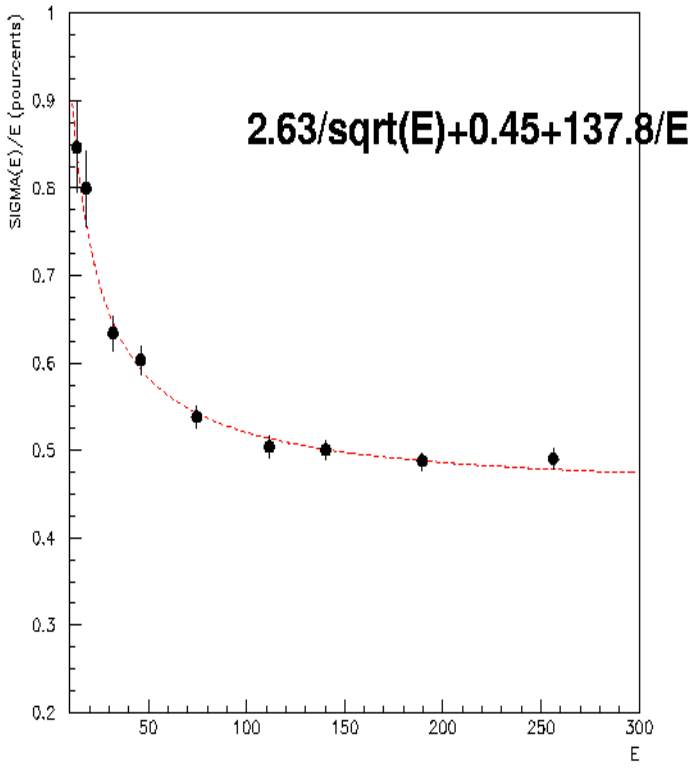

Figure 28: Energy resolution for crystal 18

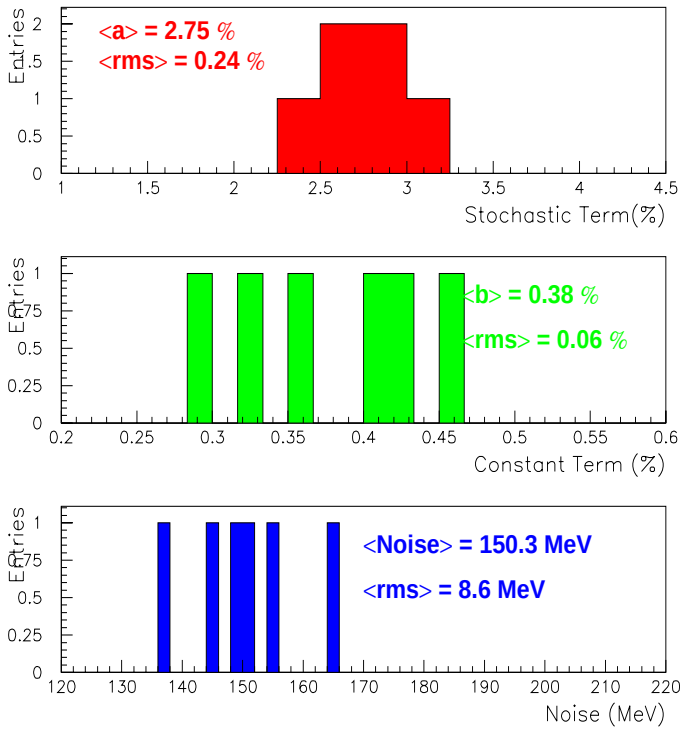

Figure 29: Distributions of energy resolution parameters for both periods combined

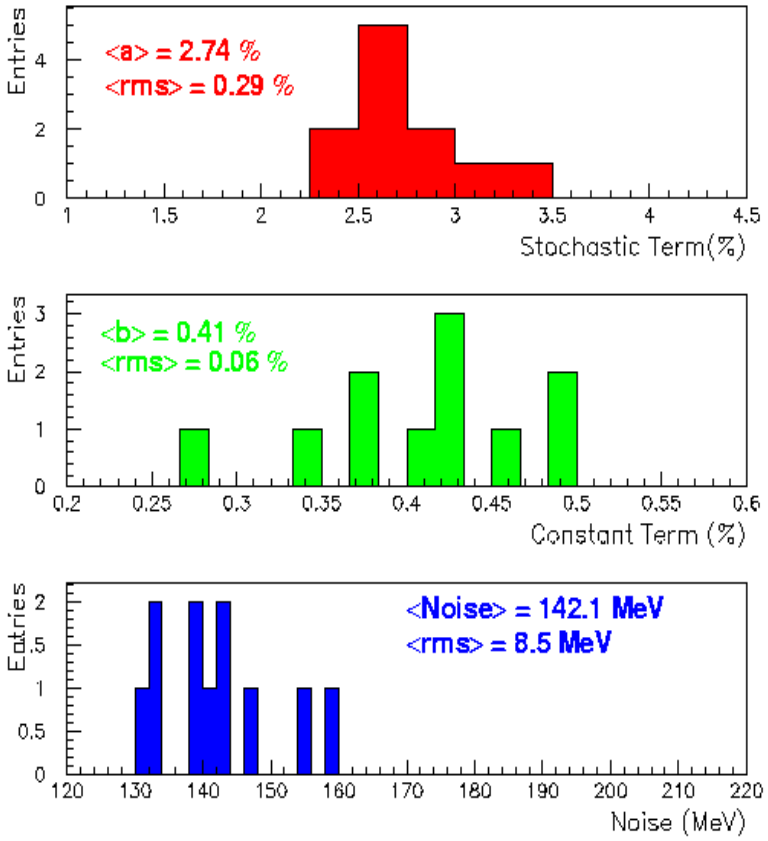

Figure 30: Distributions of energy resolution parameters for both periods combined, without the point at 280 GeV

The *mean* energy resolution for August runs, not including the point at 280 GeV, is :

$$\frac{\sigma}{E} = \frac{2.74\%}{\sqrt{E}} \oplus 0.41\% \oplus \frac{142\ MeV}{E}$$

To complement these results, we took the values of resolution and noise from all 11 channels, between 15 and 200 GeV, we do a mean of resolution and noise obtained at each energy, then fit these resolution values for this 'mean crystal'. Figure 31 shows this fit.

We remark that this *mean* resolution energy is the same as that obtained in fig. 30 :

$$\frac{\sigma}{E} = \frac{2.73\%}{\sqrt{E}} \oplus 0.42\% \oplus \frac{142\ MeV}{E}$$

5.6 Simulation and Interpretation

5.6.1 Simulation

A GEANT simulation of proto'99 exists, which has the same 3^o tilt in theta and phi with respect to the beam. We produce a simulated set of energies between 5 and 220 GeV. Figure 32 shows the resulting energy resolution calculated in the same way as for the data for a $4 \times 4\ mm^2$ beam area centered on the central crystal of the array studied.

The energy resolution for simulated prototype is :

$$\frac{\sigma}{E} = \frac{1.73\%}{\sqrt{E}} \oplus 0.21\%$$

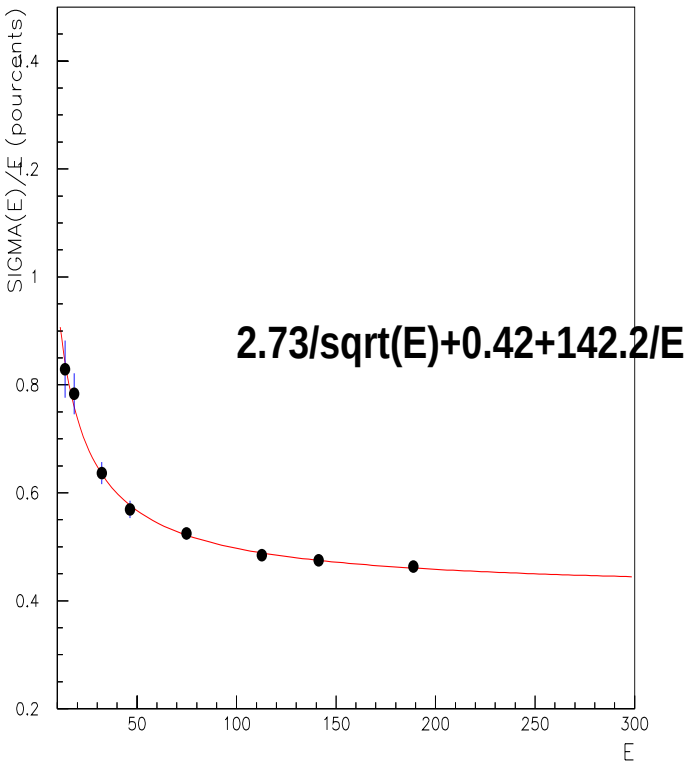

Figure 31: Energy resolution for the 'mean crystal' (the mean of 11 crystals) for both periods combined, without the point at 280 GeV

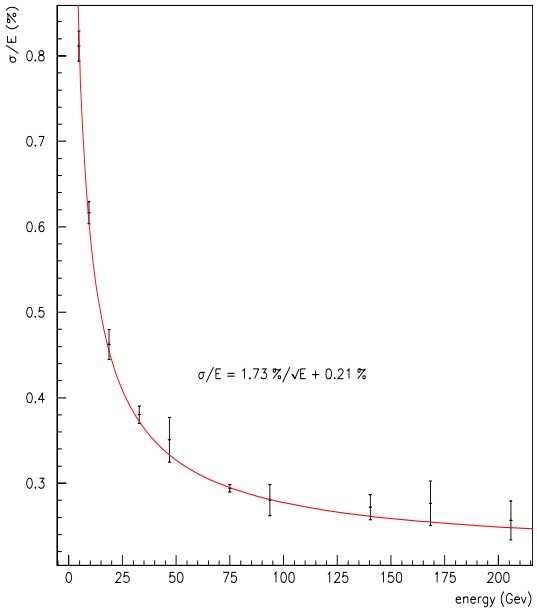

Figure 32: Energy resolution for the simulated proto'99 with $4 \times 4\ mm^2$ beam area

5.6.2 Interpretation

If we use the stochastic term of $1.73\ \%$, resulting from the simulation and we assume an excess noise factor of 2, we can estimate the light yield of crystals :

$$a(data) \ = \ a(MC) \ \oplus \ \frac{F}{N_{pe}}$$

With a mean stochastic term of $2.74 \ \pm 0.29\%$ (cf. figure 30) in data, we obtain :

$$N_{pe} \ = \ 4.43 \ \pm \ 1.56$$

This value is in good agreement with the light yield estimated by ACCOS or in situ in H4 ($5.60 \ \pm \ 0.93$) (cf. section Light Yield).

We can consider that this prototype simulation is in good agreement with the data.

So we can estimate the energy resolution in the CMS ECAL for one particle ('a pointlike beam'). Figure 33 shows the fit :

$$\frac{\sigma}{E} \ = \ \frac{1.69\%}{\sqrt{E}} \ \oplus \ 0.15\%$$

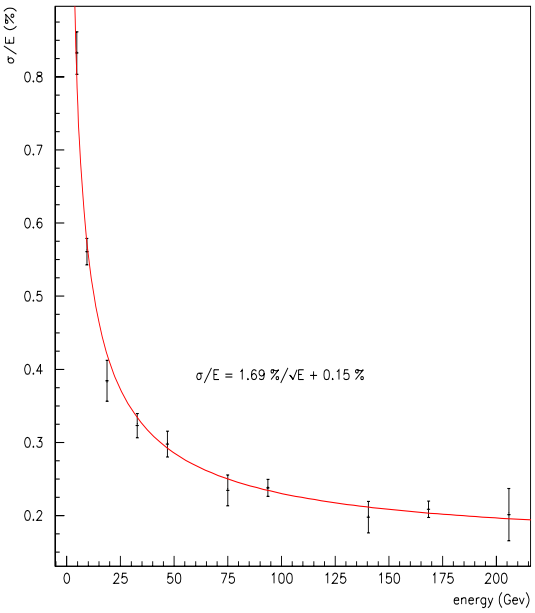

Figure 33: Energy resolution for the simulated proto'99 for a single particle

6 Position scans

6.1 Method

During the first period, we made a position scan in X and Y at $E_{beam} = 120\ GeV$ for 6 crystals in the center of the matrix (crystals 17, 18, 19 for the scan in X and crystals 13, 18 , 23 for the scan in Y). We present here the results on the scanned crystals, for the data and for a Monte-Carlo simulation. A $4 \times 4mm^2$ position cut was applied to the data. In order to see what the resolution would be in the final CMS experiment, we made some particle ('pointlike Beam") simulations.

We obtain the resolution with a 2-sigma gaussian fit of the energy reconstructed in 3×3 crystal matrix. Errors on the fit were estimated to take account the sensibility of the fit to the statistic.

6.2 Scan in X

The scan in X starts in the center of crystal 17, then it continues through crystal 18 and ends in the middle of crystal 19.

First, to verify agreement between data and simulation, we estimate energy for the considered central channel and for the sum of 9 channels. Normally, we reconstruct 76.2% and 92.8% of the beam energy (see figures 34 and 35 respectively).

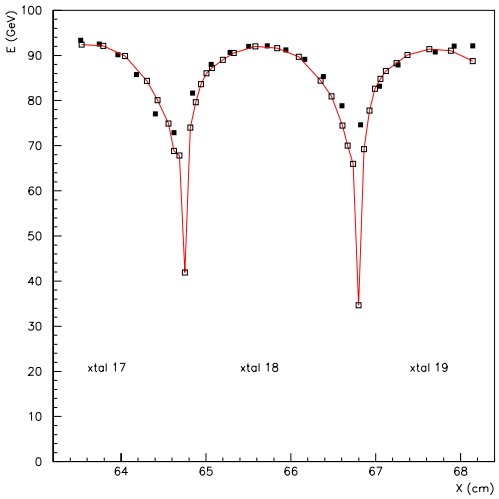

Figure 34: Scan in X on crystals 17, 18 and 19 for struck crystal , with a $4 \times 4\,mm^2$ beam. Empty squares are simulation, dark squares the data.

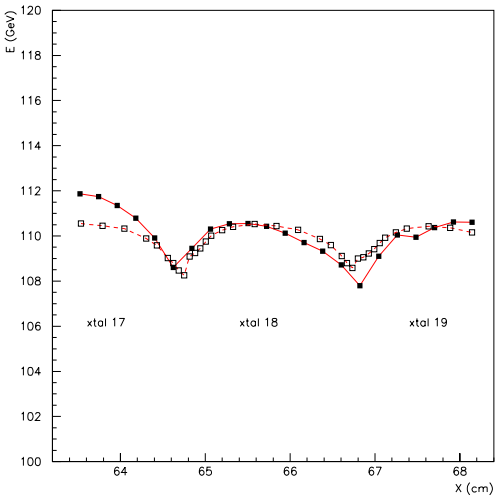

Figure 35: Scan in X on crystals 17, 18 and 19 for a 3×3 crystal matrix, with a $4 \times 4\,mm^2$ beam. Empty squares are simulation, dark squares the data.

Good agreement is observed between data and simulation (except for crystal 17).

Then we estimate the energy resolution. The results obtained with the $4 \times 4\,mm^2$ beam (figure 36 for the data and figures 37 or 38 for the simulation) show a significant degradation observe an important degradation of the resolution near the gap between crystals.

The peaks on the figures are associated with the physical transition between crystals 17/18 and 18/19. However due to the tilt of the matrix, the worst resolution values is not exactly at the transition but just a few millimeters before the crystal border.

Electronic noise and non-uniformity are not included in the simulation, but we observe approximatly the same structure of the resolution curve when we compare it to the data (2 peaks on the cracks and an improvement of the resolution when the beam hits the middle of the crystals). Noise has not been subtracted from the data.

Each crystal is 2.2 cm wide. On the figures the center of crystal 18 is around at approximatly x = 66.1 cm. The best

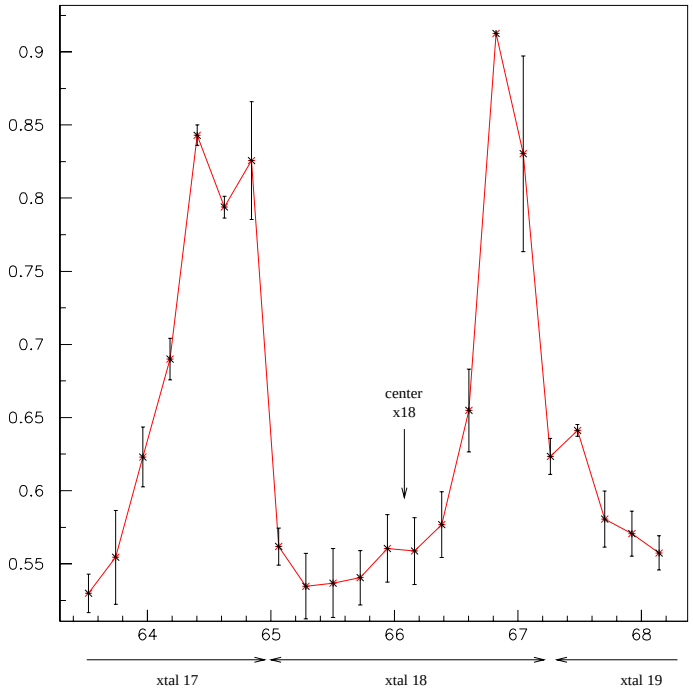

Figure 36: Energy resolution versus position in X (data) on crystals 17, 18 and 19 for the 3×3 crystal matrice, with a $4 \times 4\, mm^2$ beam. The peaks correspond to the gap between crystals.

resolution value is generally obtained for x = 65.7 cm. This difference of 4 mm between the center of the crystal and the position of best resolution is characteristic of the tilt of the matrix. In figure 37 we obtained the energy resolution by summing the energy deposited in the crystal struck by the beam and in the 8 surrounding crystals. Figure 38 shows the situation when we take a 3×3 submatrix centered on the crystal where the maximum energy is deposited.

This crystal is not necessary the same as the central crystal given by the first method, in particular near the borders of the crystal (due to the 3 degree tilt in η, when the beam hits the border of crystal 17, the electomagnetic shower energy is actually contained mostly in crystal 18). In this case we observe a splitting in the peaks. The resolution seems to increase considerably over a short distance when the beam scans the crack between two crystals.

6.3 Scan in Y

The same analysis as before is carried out for the scan in Y (crystals 13, 18 and 23). The main difference from the scan in X is that the scan in Y extends over two submodules. Crystals 13 and 18 belong to the same submodule, but crystal 23 is on a lower submodule, therefore the gap between crystal 18 and 23 is wider than the crack between crystals 13 and 18 (see table in section 'Noise by channel'). This has, of course, a direct influence on the resolution.

First, we estimate reconstructed energy (see figures 39 and 40).

Good agreement is observed between date and simulation except for the gap between submodules mentionned above.

The center of crystal 18 is located at y = -1.1 cm. As for the scan in X, the center of the crystal does not correspond to the best resolution value, due to the matrix tilt.

In addition, again as for X, the results obtained from the data (figure 41) show a significant degradation of the resolution when the beam hits the cracks of the matrix.

The greatest peak in the resolution curve corresponds to the gap between the two submodules. The resolution near the crack between 13 and 18 crystals (in the same submodule) is also globaly degraded but the scan shows a sharp improvement of this resolution right at the crossing of the 2 crystals; the peak is split in two. This somewhat counter-intuitive effect, is confirmed by the simulation (figures 42 and 43).

In figure 43 we also observe this 'brief' improvement of the resolution in the gap peaks.

When we choose the 3×3 submatrix centered on the crystal where the maximum energy is deposited (fig 43) the

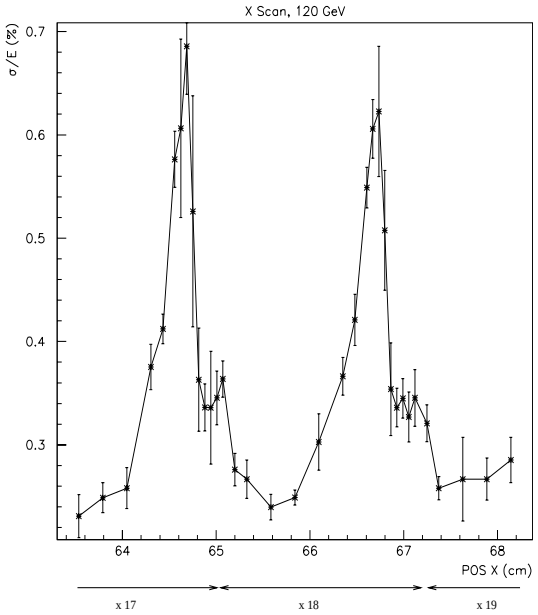

Figure 37: Energy resolution versus position in X (simulated) on crystals 17, 18 and 19, with a $4 \times 4\,mm^2$ beam, for a 3×3 crystal matrix centered on the crystal hit by the beam

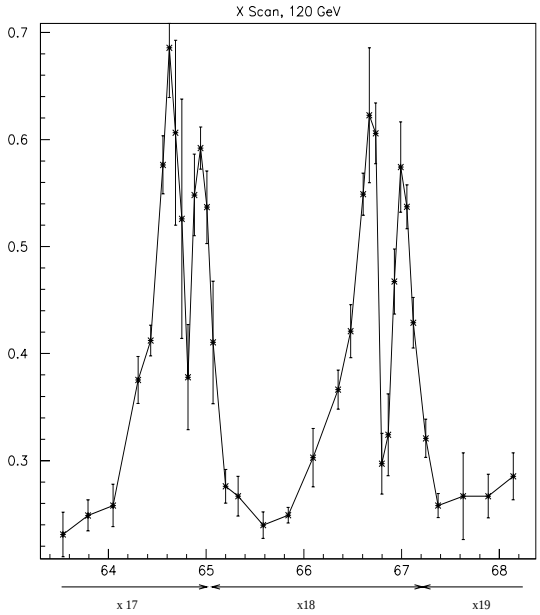

Figure 38: Energy resolution versus position in X(simulated) on crystals 17, 18 and 19 with a $4 \times 4\,mm^2$ beam, for a 3×3 crystal matrix centered on the crystal where the maximum energy is deposited

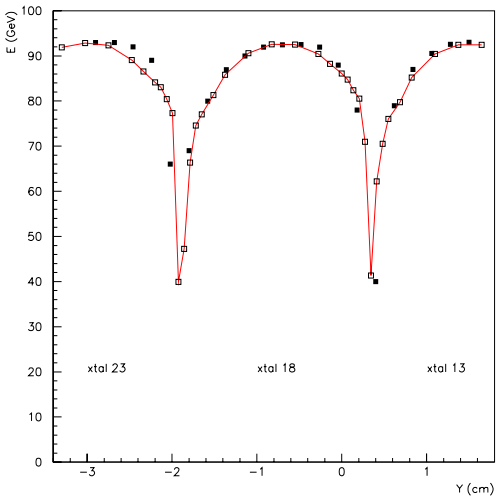

Figure 39: Scan in Y (data) on crystals 13, 18 and 23 for struck crystal , with a $4 \times 4\,mm^2$ beam. Empty squares are simulation, dark squares the data.

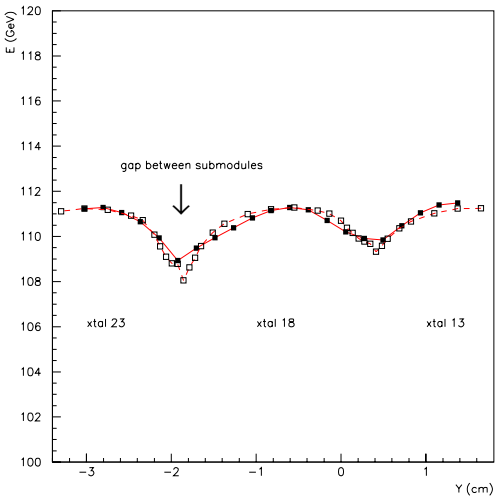

Figure 40: Scan in Y (data) on crystals 13, 18 and 23 for a 3×3 crystal matrix, with a $4 \times 4\,mm^2$ beam. Empty squares are simulation, dark squares the data.

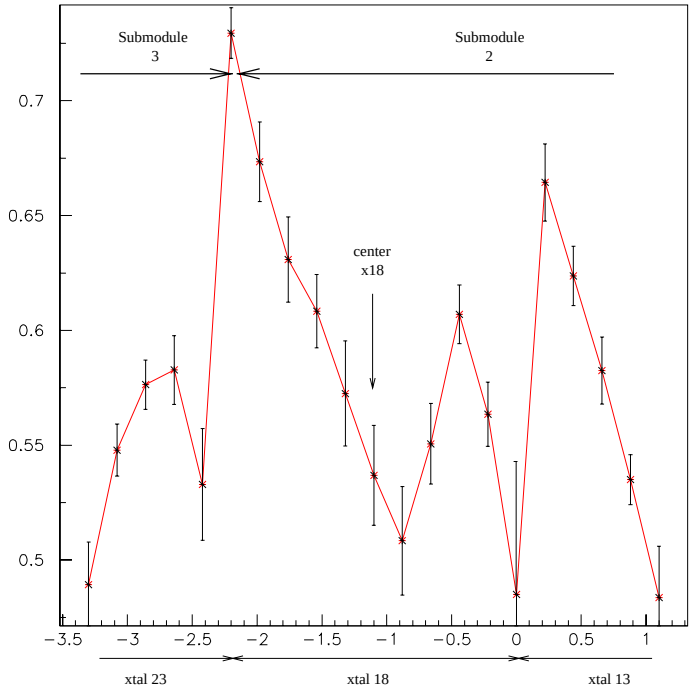

Figure 41: Energy resolution versus position in Y (data) on crystal 13, 18 and 23 for the 3×3 crystal matrix, centered on each crystal, with a $4 \times 4\,mm^2$ beam. The peaks correspond to the gap between the crystals and the highest peak correspond to the gap between two submodules.

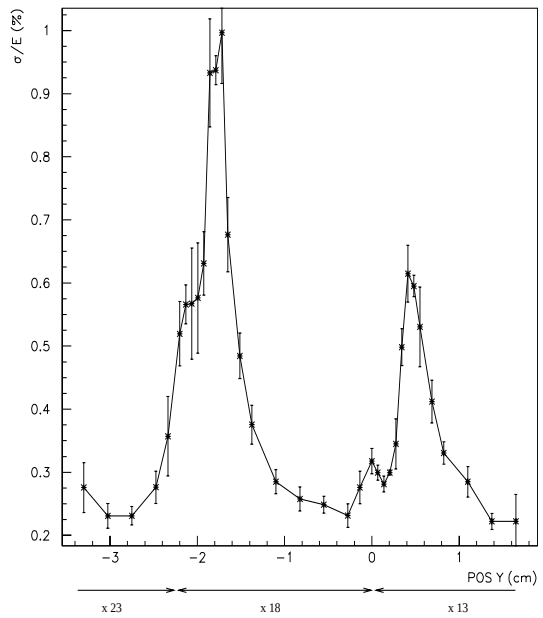

Figure 42: Energy resolution versus position in Y (simulated) on crystals 13, 18, 23 with a $4 \times 4\,mm^2$ beam, for a 3×3 crystal matrix centered on the crystal struck by the beam

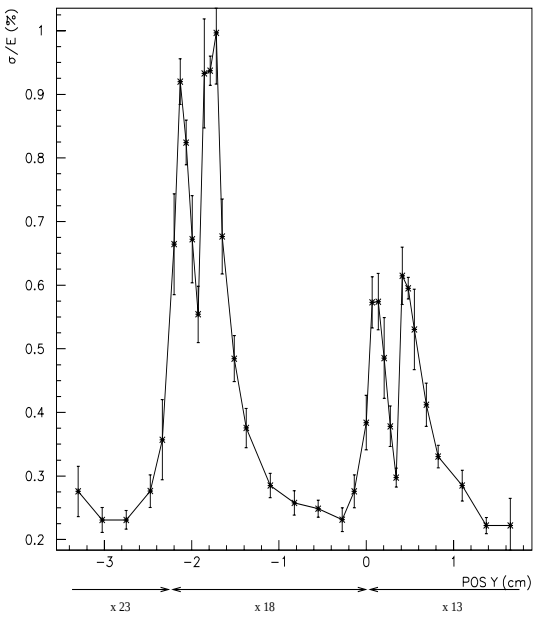

Figure 43: Energy resolution versus position in Y (simulated) on crystals 13, 18, 23 with a $4 \times 4\,mm^2$ beam, for a 3×3 crystal matrix centered on the crystal where the maximum energy is deposited

data in Y is closer to the simulation than for a submatrix centered on the crystal hit by the beam (fig. 42). We do not observe in this figure the 'splitting' of the peaks. Since we had the contrary for the scan in X, we can suppose that the data is best simulated by a mix of these two methods.

6.4 Conclusion on Positions Scans

Figures 44 and 45 show the simulated energy resolution for a single particle (pointlike beam) in a 3×3 matrix centered on the crystal and on the crystal where the maximum energy is deposited for a scan in X. The scan is made here only for the central crystal (18). We observe a lowering of the peaks, the difference between the minimum and the maximum resolution values is around 0.12% instead of 0.45% for the $4 \times 4mm^2$ beam.

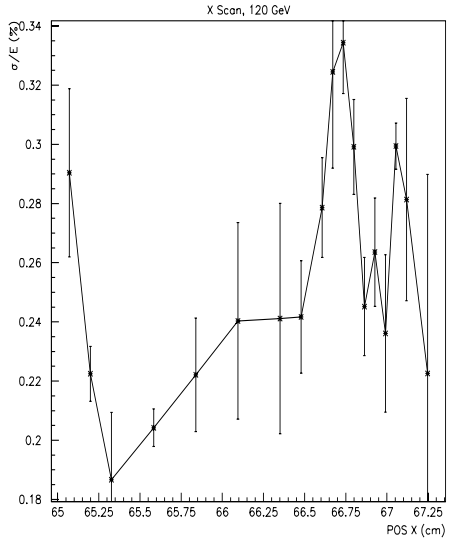

Figure 44: Energy resolution versus position in X (simulated) on crystal 18 only, with a pointlike beam, for a 3×3 crystal matrix centered on the struck crystal 18

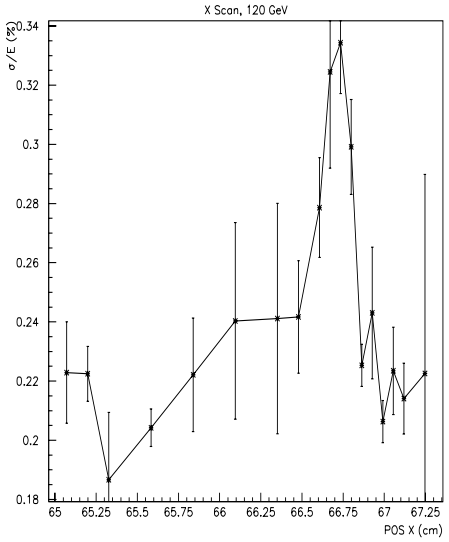

Figure 45: Energy resolution versus position in X (simulated) on crystal 18, with a pointlike beam, for a 3×3 crystal matrix centered on the crystal where the maximum energy is deposited

We have done the same simulation for a scan in Y (see figures 46 and 47). We likewise observe a lowering of the peaks, the difference between the minimum and the maximum resolution values is around 0.4% instead of 0.75% for the $4 \times 4mm^2$ beam.

The data and the simulation show an important degradation of the resolution for a 4x4 mm^2 beam in the cracks. However for a single particle (pointlike beam), which corresponds to the realistic case of detection of one photon or electron in the ECAL, the difference between the maximum and minimum resolution decreases to about 0.1%, for a scan in X. In the case of the Y scan, this difference goes up to 0.6% when we consider the crystals in different submodules. The splitting of the peaks, observed for the 4x4 mm^2 beam, in the case where the matrix is centered on the crystal where the maximum energy is deposited, seems also to disappear in the case of a single particle.

7 Conclusion

The results presented in this note demonstrate that a lead tungstate electromagnetic calorimeter is able to exhibit very good performance in terms of noise and energy resolution. In these beam tests, excellent energy resolution is now currently found with 11 crystals at the center of 9 crystal sub-matrices. The intrinsic and correlated noise was, for "classical" electronic read-out system, consistent with stated in the TDR. We have verified that simulation and data show approximately the same reconstructed energy, so we will be able to ultimately verify this result on Module 0 with 400 channels.

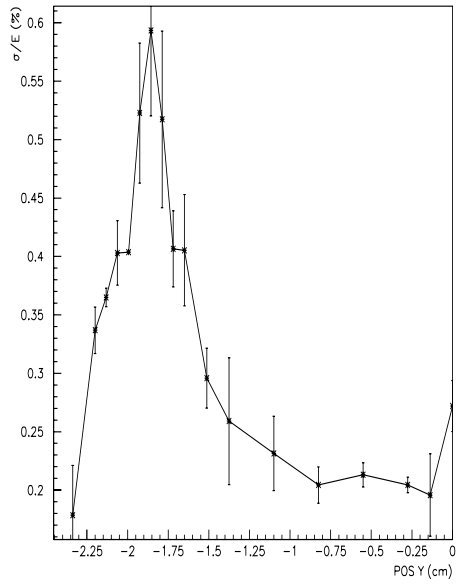

Figure 46: Energy resolution versus position in Y (simulated) on crystal 18, with a pointlike beam, for a 3×3 crystal matrix centered on the crystal struck by the beam

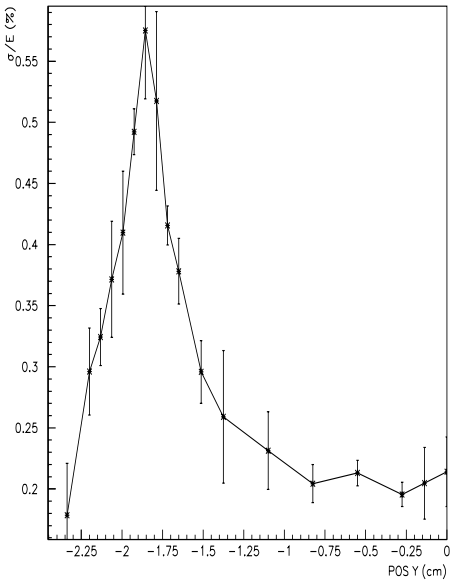

Figure 47: Energy resolution versus position in Y (simulated) on crystal 18, with a pointlike beam, for a 3×3 crystal matrix centered on the crystal where the maximum energy is deposited

Acknowledgements :

The authors thank A. Givernaud for very fruitful discussions concerning proto'99 simulation and C. Seez for interesting remarks about energy resolution determination.

We thank J.C. Mabo for giving us a Geant version of the Euclide prototype 99 design.